
Application of the Ghosh & Lamb Relation to the Spin-up/down Behavior in the X-ray Binary Pulsar 4U 1626–67

Toshihiro TAKAGI^{1,2,*}, Tatehiro MIHARA², Mutsumi SUGIZAKI², Kazuo MAKISHIMA² and Mikio MORII³

¹Department of Physics, Nihon University, 1-8-14 Kandasurugadai, Chiyoda-ku, Tokyo 101-8308, Japan

²MAXI team, RIKEN, 2-1 Hirosawa, Wako, Saitama 351-0198, Japan

³Research Center for Statistical Machine Learning, Institute of Statistical Mathematics, 10-3 Midori-cho, Tachikawa, Tokyo 190-8562, Japan

*E-mail: takagi@crab.riken.jp

Received ; Accepted

Abstract

We analyzed continuous MAXI/GSC data of the X-ray binary pulsar 4U 1626–67 from 2009 October to 2013 September, and determined the pulse period and the pulse-period derivative for every 60-d interval by the epoch folding method. The obtained periods are consistent with those provided by the Fermi/GBM pulsar project. In all the 60-d intervals, the pulsar was observed to spin up, with the spin-up rate positively correlated with the 2–20 keV flux. We applied the accretion torque model proposed by Ghosh & Lamb (1979, *ApJ*, 234, 296) to the MAXI/GSC data, as well as the past data including both spin-up and spin-down phases. The Ghosh & Lamb relation was confirmed to successfully explain the observed relation between the spin-up/down rate and the flux. By comparing the model-predicted luminosity with the observed flux, the source distance was constrained as 5–13 kpc, which is consistent with that by Chakrabarty (1998, *ApJ*, 492, 342). Conversely, if the source distance is assumed, the data can constrain the mass and radius of the neutron star, because the Ghosh & Lamb model depends on these parameters. We attempted this idea, and found that an assumed distance of, e.g., 10 kpc gives a mass in the range of 1.81–1.90 solar mass, and a radius of 11.4–11.5 km, although these results are still subject to considerable systematic uncertainties other than that in the distance.

Key words: pulsars: individual (4U 1626–67) — stars: neutron — X-rays: binaries

1 Introduction

An X-ray binary pulsar is a system consisting of a magnetized neutron star and a stellar companion. The X-ray emission is powered by gravitational energy of accreting matter. In a system with a low-mass companion star, the accretion flow is considered to take place via Roche-Lobe overflow, and to form an accretion disk in the vicinity of the pulsar. The angular momentum of the accreting gas is transferred to the pulsar at the

inner edge of the accretion disk, and accelerates the pulsar rotation until it finally reaches an equilibrium determined by the accretion rate and the magnetic moment of the pulsar. So far, numbers of theoretical studies have been performed on the interaction between the pulsar magnetosphere and the accretion flows. Along this scenario, Rappaport & Joss (1977), Ghosh & Lamb (1979) (GL79 hereafter) and Lovelace et al. (1995) (LRB95 hereafter) proposed their accretion models and pre-

sented equations describing the pulse-period derivative \dot{P} as a function of the luminosity L , the pulse period P , the mass M , the radius R and the surface magnetic field B_c of the neutron star. These models have been examined against observational data (e.g. Joss & Rappaport 1984; Finger et al. 1996; Reynolds et al. 1996; Bildsten et al. 1997; Klochkov et al. 2009; Sugizaki et al. 2015). The results show that the observed \dot{P} - L relations are grossly consistent with the model predictions. However, the validity of the models has not yet been fully confirmed, because it requires long-term monitoring of some suitable objects with known B_c , covering significant pulse-period and luminosity changes with a sufficient sampling rate.

When these models describing the accretion torque are better calibrated, the observed \dot{P} - L relations can give us observational constraints on M and R , which are very important because they are directly connected to the equation of state (EOS) of nuclear matter. So far, various observational attempts to measure M and R have been carried out, and generally yielded $M \simeq 1.4M_\odot$ and $R \simeq 12$ km (e.g. reviews by Bhattacharyya 2010 and Özel 2013). However, the measurements are not yet accurate enough to constrain the EOS. Furthermore, the values of M (mainly from X-ray binary pulsars) and R (mainly from weakly-magnetized neutron stars) have been derived from different populations of neutron stars. Therefore, further studies of the \dot{P} - L relations are expected to be valuable.

4U 1626–67 is a low-mass X-ray binary pulsar first detected with the Uhuru satellite (Giacconi et al. 1972), and its 7.6-s coherent pulsation was discovered by Rappaport et al. (1977). Because no period modulation due to orbital motion has been detected beyond an upper limit of $a_x \sin i \leq 13$ lt-ms (a_x is the orbital semi-major axis of the pulsar and i is the orbital inclination), the mass of the companion star is estimated to be very low ($\sim 0.03 - 0.09M_\odot$ for $11^\circ \leq i \leq 36^\circ$; Levine et al. 1988). It is hence classified as an ultra compact X-ray binary (van Haften et al. 2012). The BeppoSAX observation revealed a cyclotron resonance scattering feature at ~ 37 keV, indicating the surface magnetic field of $B_c = 3.2 \times 10^{12} (1 + z_g)$ G, where z_g is the gravitational redshift,

$$z_g = \left(1 - \frac{2GM}{Rc^2}\right)^{-\frac{1}{2}} - 1, \quad (1)$$

represented by the gravitational constant G and the velocity of light c (Orlandini et al. 1998). The feature was confirmed by the Suzaku observation (Iwakiri et al. 2012). The source distance was estimated to be 5–13 kpc from the optical flux by assuming that the effective X-ray albedo of the accretion disk is high ($\gtrsim 0.9$) (Chakrabarty 1998).

Since the discovery of the 7.6-s pulsation in 1977, the period of 4U 1626–67 has been repeatedly measured with various X-ray satellites (e.g. references in Chakrabarty et al. 1997; Camero-Arranz et al. 2010). Table 1 summarizes the X-ray fluxes, periods and period derivatives observed from 1978 to

2008, and figure 1 visualizes long-term behavior of these quantities. It clearly shows that the source made transitions twice between the spin-up and the spin-down phases, at MJD ~ 48000 (1990 June) and MJD ~ 54000 (2008 February), separated by ~ 18 years. In each phase \dot{P} were almost constant, and its absolute values were very similar as $|\dot{P}| = 2 \sim 5 \times 10^{-11} \text{ s s}^{-1}$. These period-change behavior suggests that 4U 1626–67 is close to an equilibrium state in which the net torque transfer from the accreting matter to the pulsar is approximately zero. At the last transition in 2008 when the source turned from the spin-down into the spin-up phase, the flux increased by a factor of ~ 2.5 (Camero-Arranz et al. 2010). These properties, together with the accurate knowledge of B_c , make this object ideal for our study.

Monitor of All-sky X-ray Image (MAXI; Matsuoka et al. 2009) is an X-ray all-sky monitor on the International Space Station. Since the in-orbit operation started in 2009 August, its main instrument, the GSC (Gas Slit Camera; Mihara et al. 2011; Sugizaki et al. 2011), has been scanning the whole sky every 92 min in the 2–20 keV band. The GSC field of view typically scans a celestial point source for about 60 s in each transit, which is long enough to study the 7.6-s pulsation from 4U 1626–67. Thus, the MAXI/GSC data are useful to study the long-term variation of the flux, P , and \dot{P} .

In this paper, we analyze the MAXI/GSC data of 4U 1626–67 from MJD 55110 (2009 October 6) to MJD 56550 (2013 September 15) and determine the flux, P , and \dot{P} . We then apply the spin-up/down models proposed by GL79 and LRB95 to the previous and the MAXI/GSC data, to examine whether either model can explain the observed behavior of 4U 1626–67, and to evaluate how these data can constrain the source distance, as well as the mass and radius of the neutron star.

2 Data Analysis

2.1 X-ray light curve with MAXI

X-ray events of 4U 1626–67 were extracted from all-sky GSC data, and accumulated over every 60-d interval from MJD 55110 (2009 October 6) to MJD 56550 (2013 September 15), using the on-demand analysis system provided by the MAXI team². We employed the standard regions to extract the on-source and background events; 2° radius circle for the source region and an annulus with inner and outer radii of $2^\circ.1$ and 3° , respectively, for the background. We fitted all the obtained spectra with a power-law model without absorption. The fits were acceptable for all the 60-d intervals, and gave photon indices of $1.0 \sim 1.3$. We calculated the 2–20 keV model flux, and present in figure 2a its variation over the 4 years analyzed, where errors refer to 1σ statistical uncertainties. The flux was thus almost

¹ <http://gammaray.nsstc.nasa.gov/batse/pulsar/data/sources/4u1626.html>

² <http://maxi.riken.jp/mxondem>

Table 1. X-ray flux, period and period derivative obtained in past observations of 4U 1626–67.

Observation Date	Flux				Pulsation			Ref. [‡]
	Period (MJD)	Band (keV)	Obs. (10^{-10} erg s $^{-1}$ cm $^{-2}$)	Bolometric* (10^{-10} erg s $^{-1}$ cm $^{-2}$)	Epoch (MJD)	P^\dagger (s)	\dot{P} (10^{-11} s s $^{-1}$)	
1978 Mar	43596	0.7–60	24 ± 3	25 ± 3	43596.7	7.679190(26)	-4.55^\S	1
1979 Feb	43928–43946	2–10	5.1 ± 0.3	19 ± 1	43946.0	7.677632(13)	$-4.9 \pm 0.1^\S$	2
1983 May	45457–45459	2–20	10.1 ± 0.2	19.0 ± 0.4	45458.0	7.671350(1)	-13 ± 5	3
1983 Aug	45576	2–10	5.6 ± 0.5	20.3 ± 1.8	45576.9	7.67077(1)	-5.65 ± 0.10^l	4
1986 Mar	46519–46520	1–20	$14 \pm 0.4^\#$	22 ± 0.7	46520.0	7.6664220(5)	$-4.96 \pm 0.06^\S$	5
1987 Mar	46855–48012	1–20	8.89 ± 0.56	14.0 ± 0.9				6
1988 Aug					47400.3	7.6625685(30)		7
1990 Apr	47999–48002	2–60	~ 20.6	~ 24.7	48001.1	7.660069(2)		8
1990 Jun	48043–48530	1–20	6.67 ± 0.89	10.9 ± 1.5				6
1990 Aug					48133.5	7.66001(4)		4
1993 Aug	49210–49211	0.5–10	~ 2.8	~ 9.9				9
1996 Aug	50301–50306	2–60	~ 6.1	~ 6.5				10
2000 Sep	51803	0.3–10	2.4**	8.4	51803.6	7.6726(2)		11
2001 Aug	52145	0.3–10	1.8**	6.3	52145.1	7.6736(2)	3.39 ± 0.96^l	11
2003 Jun	52793	0.3–10	1.8**	6.3	52795.1	7.67514(5)	2.74 ± 0.37^l	11
2003 Aug	52871	0.3–10	1.6**	5.6	52871.2	7.67544(6)	4.6 ± 1.2^l	11
2007 Jun	54280	15–50	2.8 ± 0.1	5.6 ± 0.2	54280	~ 7.6793	2.9	12
2007 Sep	54370	15–50	2.6 ± 0.1	5.2 ± 0.2	54370	~ 7.6793	2.7	12
2007 Dec	54450	15–50	4.0 ± 0.1	8.0 ± 0.3	54450	~ 7.6793	1.9	12
2008 Jan	54480	15–50	4.6 ± 0.2	9.3 ± 0.4	54480	~ 7.6793	0.18	12
2008 Feb	54510	15–50	4.6 ± 0.1	11.5 ± 0.3	54510	~ 7.6793	-0.53	12
2008 Mar	54530	2–100	10.1 ± 0.8	11.7 ± 0.9				13
2008 Mar	54550	15–50	5.8 ± 0.1	14.5 ± 0.3	54550	~ 7.6793	-2.3	12
2008 Jun	54620	15–50	5.9 ± 0.1	14.8 ± 0.2	54620	~ 7.6793	-2.7	12

All errors represent $1\text{-}\sigma$ uncertainties.

* Converted 0.5–100 keV flux, assuming the spectral models in Camero-Arranz et al. (2012).

† Values in parentheses are 1σ error in the last digit(s).

‡ (1) Pravdo et al. (1979) (HEAO 1/A-2), (2) Elsner et al. (1983) (Einstein/MPC), (3) Kii et al. (1986) (Tenma), (4) Mavromatakis (1994) (EXOSAT/GSPC, ROSAT), (5) Levine et al. (1988) (EXOSAT/ME), (6) Vaughan & Kitamoto (1997) (Ginga/ASM), (7) Shinoda et al. (1990) (Ginga), (8) Mihara (1995) (Ginga), (9) Angelini et al. (1995) (ASCA), (10) Orlandini et al. (1998) (BeppoSAX), (11) Krauss et al. (2007) (Chandra, XMM-Newton), (12) The data were read from figure 4 in Camero-Arranz et al. (2010) (Swift/BAT), (13) Camero-Arranz et al. (2010) (RXTE/PCA spectra).

§ Averaged value.

^l Averaged \dot{P} calculated from P of the observation and the previous one in this table.

The error was estimated by the count rate with ME, using the values of the count rate and the error with GSPC.

** Absorption-corrected flux.

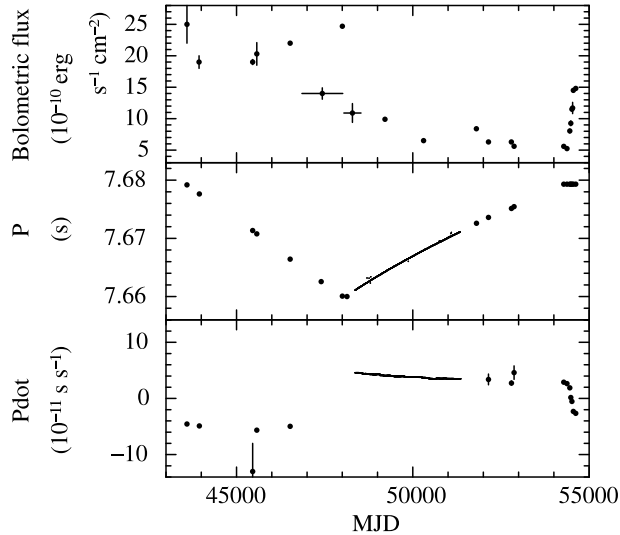


Fig. 1. Bolometric flux (top), period (middle) and period derivative (bottom) of 4U 1626–67 obtained by past X-ray observations from 1978 to 2008. In the top panel, observed X-ray intensities are converted to the model flux in the 0.5–100 keV band assuming the typical spectral model given by Camero-Arranz et al. (2012). Filled circles and solid lines represent the past observations in table 1 and BATSE¹ observations, respectively.

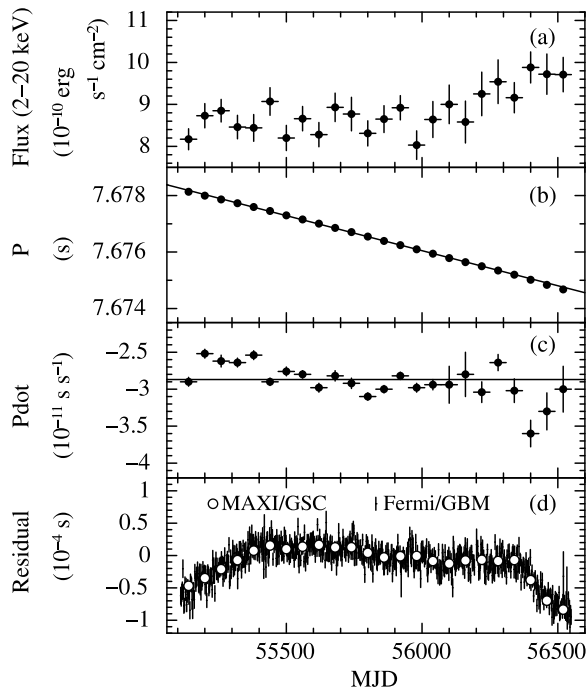


Fig. 2. The 2–20 keV flux (panel a), the period (panel b), and the period derivative (panel c) of 4U 1626–67, obtained every 60 d with the MAXI/GSC data from 2009 October to 2013 September. Panel (d) shows residuals from the best-fit linear function to the period data in (b). The horizontal line in (c) represents the slope of the line in (b) ($-2.87 \times 10^{-11} \text{ s s}^{-1}$). The Fermi/GBM results are superposed by vertical line segments.

constant at $\sim 8.6 \times 10^{-10} \text{ erg cm}^{-2} \text{ s}^{-1}$ before MJD 56200, and slightly increased to $\sim 9.5 \times 10^{-10} \text{ erg cm}^{-2} \text{ s}^{-1}$ after that time.

2.2 Pulse periods and pulse-period derivatives with MAXI

The pulsar timing analysis of 4U 1626–67 was carried out with the GSC event data of revision 1.5, which have a time resolution of $50 \mu\text{s}$. We extracted events within a $1^\circ.5$ radius from the source position, and then applied the barycentric correction to their arrival times. Background was not subtracted in the timing analysis. To determine P and \dot{P} , we employed the epoch folding method. There, χ^2 of the folded pulse profile, defined as

$$\chi^2 = \sum_{i=1}^n \left[\frac{(y_i - \bar{y})}{\sqrt{y_i}} \right]^2, \quad \bar{y} = \frac{\sum (\frac{1}{\sqrt{y_i}})^2 y_i}{\sum (\frac{1}{\sqrt{y_i}})^2}, \quad (2)$$

is calculated for each trial value of P and \dot{P} , where n is the number of bins of the folded profile and y_i is the number of events in the i -th bin. We used $n = 32$, and confirmed that the exposure is uniform over the 32 bins within 0.5%. The epoch-folding analysis was performed for every 60-d interval, to be coincident with the light-curve time bins employed in section 2.1. In each interval, we searched for the values of P and \dot{P} that maximize χ^2 . Here, the P and \dot{P} values measured with the Fermi/GBM pulsar project³ were used to select the search ranges, and \dot{P} was assumed constant in each interval. Figure 3 shows the obtained χ^2 values on the P – \dot{P} plane, employing MJD 55290–55350 as a typical example. The $1\text{-}\sigma$ errors of P and \dot{P} were estimated by Monte-Carlo simulations (see Appendix 3). We repeated the analysis in the energy bands of 2–20 keV, 2–10 keV, 2–4 keV, 4–10 keV and 10–20 keV, and then selected the results of the 2–10 keV band because the maximum χ^2 was the highest among them. Results from the other energy bands were consistent with these.

Figure 2b and 2c show time variations of the obtained P and \dot{P} , respectively. The absolute value of \dot{P} increased with the flux increase around MJD 56400. We fitted the data in figure 2b with a linear function, because their distribution appears quite linear. The best-fit slope was then obtained as $\langle \dot{P} \rangle = -2.87 \times 10^{-11} \text{ s s}^{-1}$. Figure 2d shows the residuals from the best-fit line, where the results of the Fermi/GBM pulsar data are overlaid. The results of the MAXI/GSC and the Fermi/GBM are found to agree with each other within the errors.

2.3 Estimation of bolometric flux

In the following sections, we apply the theoretical models of pulsar spin-up/down, proposed by GL79 and LRB95, to the ob-

³ <http://gammaray.nsstc.nasa.gov/gbm/science/pulsars/lightcurves/4u1626.html>

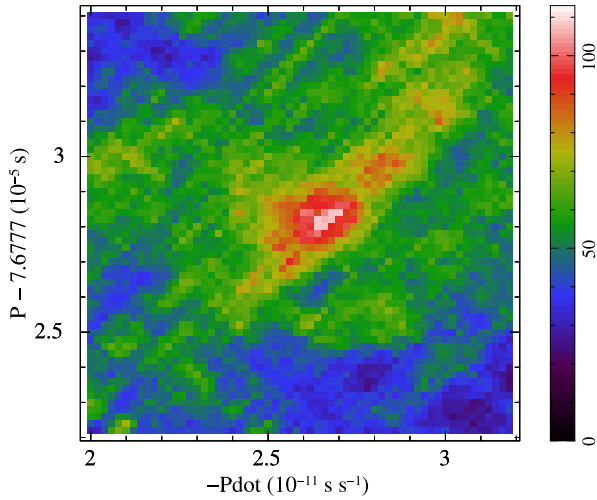


Fig. 3. Distribution of χ^2 of the folded pulse profiles, shown as a function of the trial P and \dot{P} , obtained from the 2–10 keV MAXI/GSC event data in MJD 55290–55350. The right bar indicates the χ^2 values. The maximum χ^2 is 108 for 31 degrees of freedom at $P = 7.6777282$ s and $\dot{P} = -2.64 \times 10^{-11}$ s s $^{-1}$.

served data including those from the previous measurements and from the MAXI/GSC. For this, we have to estimate the bolometric flux F_{bol} of the individual observations, considering different energy bands used in different observations, and employing appropriate spectral models.

The energy spectrum of 4U 1626-67 were studied in both the spin-up and spin-down phases (table 1), and the changes in the spectral shape between these two phases were reported (e.g. Jain et al. 2010; Camero-Arranz et al. 2012). According to Camero-Arranz et al. (2012), the spectra in both phases can be fitted with a model composed of a blackbody and a cutoff power law, and their difference is in the blackbody component, whose temperature is ~ 0.5 keV in the spin-up phase and ~ 0.2 keV in the spin-down phase. We hence employed these respective spectral models for the spin-up and spin-down phases, and converted the 2–20 keV MAXI/GSC flux to those in the 0.5–100 keV band, which we identify with F_{bol} . Since the power-law continuum is flat (photon index ~ 1) below ~ 20 keV and exponentially cuts off above ~ 20 keV, the fluxes in the energy band below 0.5 keV and above 100 keV are negligible. For example, the conversion factor from the 2–20 keV flux observed by the MAXI/GSC (in the spin-up phase) to the 0.5–100 keV flux is 1.88. In a similar way, we calculated F_{bol} in the past observations, and present the results in table 1.

In figure 4, we plot the relation between the observed \dot{P} and the calculated F_{bol} , including the past data. It clearly shows their negative correlation, expected from the pulsar spin up due to the accretion torque. Furthermore, the data points in the spin-up and spin-down phases apparently defines a well-defined single dependence on F_{bol} .

3 Application of the Ghosh & Lamb relation

As reviewed in section 1, GL79 derived a relation between \dot{P} and L in accreting X-ray pulsars, assuming that the accreting matter transfers its angular momentum to the pulsar at the “outer transition zone”, r_0 [equation (A2)]. The equations we used are summarized in Appendix 1. Rappaport & Joss (1977) also proposed an almost equivalent equation. Since their model equation includes an unknown parameter ($\xi v_r/v_{\text{ff}}$), of which the relation to $n(\omega_s)$ in the GL79 relation is calculable. Therefore, we employ the GL79 relation.

3.1 Model equations relating \dot{P} to the flux

According to GL79, \dot{P} is expressed by

$$\dot{P} = -5.0 \times 10^{-5} \mu_{30}^{\frac{2}{7}} n(\omega_s) S_1(M) P^2 L_{37}^{\frac{6}{7}} \text{ s yr}^{-1}, \quad (3)$$

where μ_{30} is the magnetic dipole moment μ in units of 10^{30} G cm 3 , and L_{37} is L in units of 10^{37} erg s $^{-1}$. The functions $n(\omega_s)$ and $S_1(M)$ are given in Appendix 1, where ω_s is the fastness parameter defined by equation (A6). If ω_s is in the range of 0–0.9, $n(\omega_s)$ is approximated by equation (A4) within 5%. Since $n(\omega_s)$ changes from positive to negative depending on ω_s (figure 7), \dot{P} can become both positive ($\omega_s > 0.349$; spin down) and negative ($\omega_s < 0.349$; spin up).

As shown in equation (A5), $S_1(M)$ contains the effective moment of inertia I . It is expressed as a function of M and R , dependent on the EOS. We utilize its approximation given by Lattimer & Schutz (2005),

$$I \simeq (0.237 \pm 0.008) M R^2 \times \left[1 + 0.42 \left(\frac{M}{M_{\odot}} \right) \left(\frac{R}{10 \text{ km}} \right)^{-1} + 0.009 \left(\frac{M}{M_{\odot}} \right)^4 \left(\frac{R}{10 \text{ km}} \right)^{-4} \right], \quad (4)$$

which is applicable in most of the major EOS models if $M/R \gtrsim 0.07 M_{\odot} \text{ km}^{-1}$.

In 4U 1626–67, the surface magnetic field is known from the cyclotron resonance scattering feature as $B_c = 3.2 \times 10^{12} (1 + z_g)$ G (section 1). It is considered to represent the field strength near the magnetic poles. Assuming that the magnetic axis is aligned to the pulsar rotation axis, μ at the equator in the GL79 model is represented by

$$\mu = \frac{1}{2} B_c R^3. \quad (5)$$

If the source emission is isotropic, L is calculated from F_{bol} and the distance D as

$$L = 4\pi D^2 F_{\text{bol}}. \quad (6)$$

Since the pulsar emission is anisotropic, it is not exactly correct. We employ this approximation and then discuss the effect later.

Combining equations (3), (4), (5), and (6), as well as the expression for z_g [equation (1)], we obtain a theoretical model

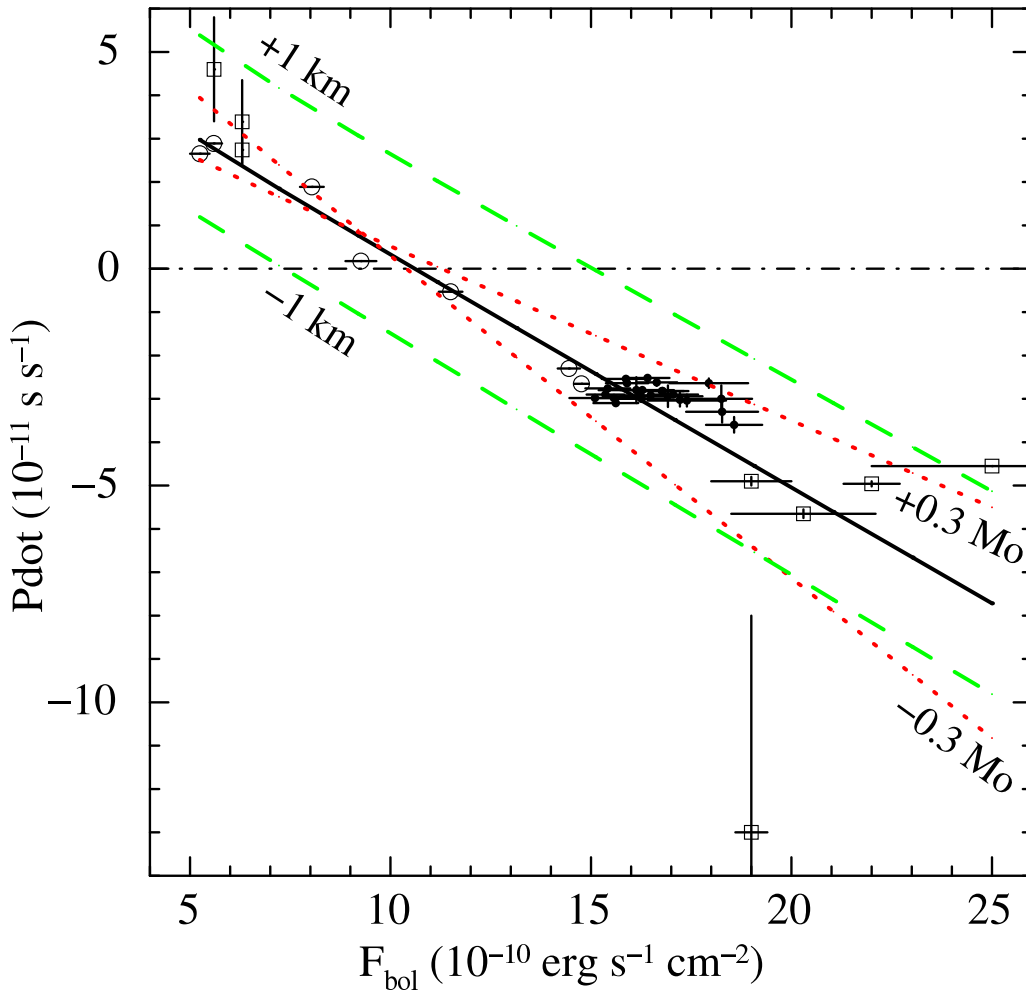


Fig. 4. A relation between \dot{P} and F_{bol} by the MAXI/GSC and the past observations. Filled circles, open circles and squares represent the MAXI/GSC data, the Swift/BAT data and the others in table 1, respectively. The dashed-dotted horizontal line indicates $\dot{P} = 0$. The solid line is the best fit model calculated by equation (3), assuming a distance of 10 kpc. The parameters are $M = 1.83 M_{\odot}$ and $R = 11.4$ km, with χ_{ν}^2 of 2.9 for 37 degrees of freedom. Dashed two lines show the case when R is changed by ± 1 km with M kept unchanged, while dotted two lines those when M is varied by $\pm 0.3 M_{\odot}$ with R fixed at 11.4 km.

equation to describe the observed \dot{P} - L relation, including three unknown parameters, D , M and R .

3.2 Comparison between the data and theory

In order to determine the possible parameter ranges of D , M and R , we fitted the observed \dot{P} - F_{bol} relation in figure 4 with the model prepared as above. When errors associated with some past measurements of \dot{P} are unavailable, we assumed an arbitrarily small value ($\Delta\dot{P} = 6 \times 10^{-16} \text{ s s}^{-1}$), because the overall errors are dominated by those in F_{bol} . This treatment was confirmed to little affect the fitting results. Since it is difficult to constrain all the three parameters simultaneously from the \dot{P} - F_{bol} relation alone, we first assumed the source distance D to be some values from 3 to 20 kpc, and then determined the allowed M - R regions as a function of the assumed distance. As an example, the fitting result assuming $D = 10$ kpc is shown in figure

4, where the best fit values were obtained as $M = 1.83 M_{\odot}$ and $R = 11.4$ km (errors are considered later).

To understand how the model curve depends on M and R , we show in figure 4 some predictions by equation (3) when either M or R is slightly changed. Thus, changes in R (with D and M fixed) causes parallel displacements of the model with little changes in its slope, while those in M (with D and R fixed) appears mainly in slope changes with the “zero-cross” point not much affected. In other words, the observed \dot{P} - F_{bol} relation has essentially two degrees of freedom, namely, the zero-cross point and the slope, and their joint use allows us to simultaneously constrain two (in the present case M and R) out of the three model parameters: the other one (D in the present case) remains unconstrained. Below, let us consider physical meanings behind this model behavior.

In figure 4, the zero-cross point at the spin-up/down threshold represents a torque-equilibrium condition, wherein so-

called co-rotation radius, which is almost uniquely determined by the observed P (with some dependence on M), can be equated with magnetospheric radius, or the outer-transition radius r_0 in the GL79 model (Appendix 1). At this radius, the gravitational pressure calculated from $L \propto D^2 F_{\text{bol}}$ should balance the magnetic pressure, and this condition specifies the value of μ . By further comparing this μ with the accurately measured B_c , we can constrain R via equation (5). As a result, the zero-cross point becomes more sensitively to R rather than to M . More quantitatively, the torque-equilibrium condition in equation (A6), $\omega_s = 0.349$, can be combined with equation (5), to yield a scaling for the flux at the torque equilibrium as

$$F_{\text{bol}} \propto M^{-\frac{2}{3}} R^5 D^{-2}, \quad (7)$$

where dependences on B_c and P were omitted.

The slope of the \dot{P} - F_{bol} relation in figure 4 means the conversion factor from an increment of the luminosity (and hence of the accretion torque) to that in the neutron-star rotation. Thus, it is inversely proportional to I , so that an increase in M will make the slope smaller (in the absolute value). A larger R will act in the same sense through I , but this effect is partially canceled by an induced increase in μ , through equation (3), which would make period changes easier. As a result, the slope becomes mainly determined by M . Quantitatively, at the highest spin-up regime which most accurately specifies the slope, we can approximate $\omega \rightarrow 0$, and hence $n(\omega_s) \sim \text{constant}$ from figure 7, to rewrite equation (3) as

$$-\dot{P} \propto M^{-\frac{10}{7}} R^{-\frac{2}{7}} L^{\frac{6}{7}} \propto M^{-\frac{10}{7}} R^{-\frac{2}{7}} D^{\frac{12}{7}} F_{\text{bol}}^{\frac{6}{7}} \quad (8)$$

when ignoring the higher-order terms in equation (4). This yields the slope as

$$-\frac{d\dot{P}}{dF_{\text{bol}}} \propto M^{-\frac{10}{7}} R^{-\frac{2}{7}} D^{\frac{12}{7}} F_{\text{bol}}^{-\frac{1}{7}}. \quad (9)$$

By changing the assumed D , we calculated the best-fit M and R , and show their locus as a solid line in figure 5, where the mass-radius relations from representative EOSs [SLy (Douchin & Haensel 2001), APR (Akmal et al. 1998) and Shen (Shen et al. 1998a; Shen et al. 1998b) presented in Yagi & Yunes (2013)] are also shown. In order for the derived M and R fall in the nominal neutron-star parameters range, $M = (1.0 - 2.4) M_{\odot}$ and $R = 8.5 - 15$ km (e.g. Bhattacharyya 2010; Özel 2013), the distance must be $D = 5 - 13$ kpc. This is in a good agreement with Chakrabarty (1998). For reference, the locus in figure 5 can be analytically calculated in the following way. When a value of D is given, the measured zero-point flux specifies $M^{-2/3} R^5 D^{-2}$ via equation (7), while the slope in figure 4 specifies $M^{-10/7} R^{-2/7} D^{12/7} F_{\text{bol}}^{-1/7}$ via equation (9). By eliminating D from these two scalings, and ignoring the weakly varying factor $F_{\text{bol}}^{-1/7}$, we obtain

$$M \propto R^2 \quad (10)$$

which approximately agrees with the locus in figure 5.

In figure 4, the best-fit reduced chi-squared, $\chi_{\nu}^2 = 2.9$ for $\nu = 37$ degrees of freedom (DOF), is not within the acceptable range. One possible cause for this large χ^2 may be systematic errors on the observed fluxes, because the flux data taken from various past results must be subject to cross-calibration uncertainties among the different instruments employed. We thus repeated the model fitting by gradually increasing the systematic errors in the flux from 1%, to find that $\chi_{\nu}^2 \sim 1$ is attained if the systematic errors are set at 5.5%. This number is quite reasonable, because the fluxes of the Crab nebula measured by these instruments scatter by $\sim 10\%$ (Kirsch et al. 2005) most likely due to uncertainties in the absolute photometric sensitivities of these instruments.

Since the fit χ_{ν}^2 was found to depend little on D , we have decided to employ the systematic error of 5.5% throughout, and calculated the statistically allowed M - R region at the 68% confidence limits (χ^2 increment $\Delta\chi^2 < 2.3$ for 2 DOF). In figure 5, the obtained allowed region is indicated by a pair of dashed lines, and the ranges of M and R for representative distances of 6, 7, 8, ..., 13 kpc are listed in table 2.

3.3 Systematic uncertainties

Although the present model fitting has been found to have a capability of rather accurately constraining M and R when D is given, the uncertainty range in figure 5 (dashed lines) considers only statistical errors. We therefore need to evaluate systematic errors associated with several assumptions and approximations which we have employed. Among them, the approximations involved in equation (A4) for $n(\omega_s)$ of the GL79 model, and equation (4) for I , are considered to be accurate to within $< 5\%$ (GL79) and $< 10\%$ (Lattimer & Schutz 2005), respectively. We hence neglecting these effects, and consider below more dominant sources of systematic errors.

One obvious uncertainty is in equation (6), which assumes that the time-averaged flux of a pulsar is identical to the average over the whole direction. Although the difference between these two averages has not been estimated in 4U 1626-67, Basko & Sunyaev (1975) examined this issue in Her X-1, a similar low-mass X-ray binary pulsar, and concluded that the difference is at most 50%. Assuming that the condition is similar in 4U 1626-67, we assign a systematic uncertainty to the flux up to $\sim 50\%$, which is transferred almost directly to that in the normalization factor of equation (3). Another uncertainty inherent to the GL79 model is those in the accretion geometry, including the exact location of the ‘‘outer transition zone’’ radius r_0 of equation (A2), and the angles among the pulsar’s rotation axis, its magnetic axis, and the accretion plane; we assumed that the rotation and magnetic axes are parallel, and are perpendicular to the accretion plane. All these effects may be represented effectively by

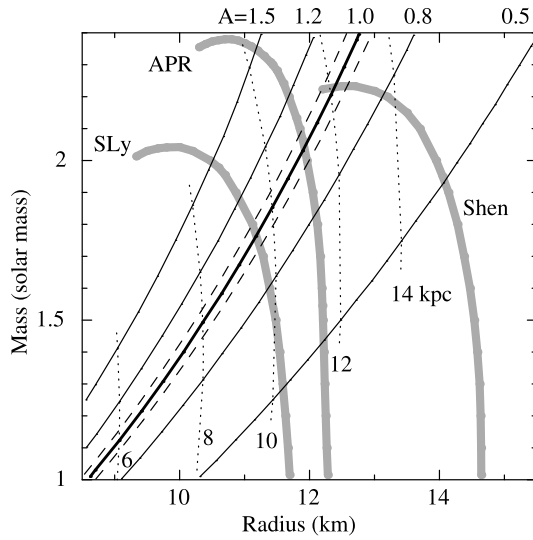


Fig. 5. Various constraints on the neutron star parameters, shown on the mass-radius plane. The solid lines indicate how the best-fit values of M and R , allowed by the data in figure 4, vary as D is changed. The cases of four different values of the normalization factor A are shown. A pair of dashed lines represent 68% errors for the $A = 1.0$ curve, while dotted lines give contours of the source distance to 4U 1626–67. The gray solid lines are mass-radius relations predicted by three EOSs; SLy, APR and Shen.

Table 2. Allowed M – R regions of the neutron star of 4U 1626–67 for an assumed distance corresponding to the dashed lines in figure 5

Assumed distance (kpc)	Mass* (M_{\odot})	Radius* (km)
6.0	1.09–1.15	9.03–9.11
7.0	1.28–1.34	9.70–9.79
8.0	1.45–1.53	10.3–10.4
9.0	1.63–1.71	10.9–11.0
10.0	1.81–1.90	11.4–11.5
11.0	1.98–2.08	11.8–12.0
12.0	2.15–2.26	12.2–12.4
13.0	2.32–2.43	12.6–12.8

* 68% confidence (2-parameters errors) limits.

uncertainty in μ_{30} . Because r_0 is proportional to $\mu_{30}^{4/7}$ and the right hand side of equation (3) to $\mu_{30}^{2/7}$, an uncertainty in μ_{30} by, e.g., 50%, would induce a 25% change in the coefficient of equation (3).

To jointly take into account all these uncertainties, we have decided to introduce an artificial normalization factor A , and multiplied it to the right hand side of equation (3). Then, the model fitting was repeated by changing A from 0.5 to 1.5. In figure 5, the allowed M – R regions for $A = 0.5, 0.8, 1.2,$ and 1.5 are also drawn. Thus, the uncertainty indeed affects the mass determination, but R remains very well constrained as long as D is somehow determined.

4 Application of the Lovelace model

As described in section 1 and detailed in Appendix 2, LRB95 developed another (in a sense more sophisticated) model, to be called “Lovelace model” here, to explain the relation between \dot{P} and L , assuming magnetic outflows and/or magnetic braking. Using the “turnover radius” r_{to} [equation (A8)] and the co-rotation radius r_{cr} [equation (A9)], the model predicts spin-up with outflows when $r_{to} < r_{cr}$, and provides both spin-up and spin-down solutions with magnetic braking by the disk when $r_{to} > r_{cr}$. To explain both the spin-up and spin-down behavior of 4U 1626–67 with the LRB95 model, $r_{to} > r_{cr}$ must therefore be satisfied in the spin-down phase. However, in the spin-down phase of 4U 1626–67, we found that $r_{to} > r_{cr}$ is not satisfied under the parameters which we assumed. For example, the values are estimated to be $r_{to} = 1.3 \times 10^8$ cm and $r_{cr} = 7.0 \times 10^8$ cm with $F_{bol} = 9.3 \times 10^{-10}$ erg cm $^{-2}$ s $^{-1}$, $M = 1.73M_{\odot}$, $R = 11.1$ km, $D = 6$ kpc, and $\alpha D_m = 0.01$. Thus, the Lovelace model cannot explain the spin-down phase of 4U 1626–67.

Even though the Lovelace model has the above problem, it might provide a reasonable explanation to the spin-up behavior of 4U 1626–67. Because $r_{to} < r_{cr}$ is satisfied in the spin-up phase of this object, we should employ the “spin-up with outflows” solution by LRB95, which describes the \dot{P} – L relation as

$$\dot{P} \approx -4.3 \times 10^{-5} \mu_{30}^{0.285} \left(\frac{\alpha D_m}{0.1} \right)^{0.15} R_6^{0.85} \times \left(\frac{M}{M_{\odot}} \right)^{-0.425} I_{45}^{-1} P^2 L_{37}^{0.85} \text{ s yr}^{-1}, \quad (11)$$

where α is the viscous parameter in Shakura & Sunyaev (1973), D_m is the magnetic diffusivity parameter, R_6 is R in units of 10^6 cm, and I_{45} is I in units of 10^{45} g cm 2 . In LRB95, α is assumed to be 0.01 to 0.1 and D_m to be of order of unity. Equation (11) is equivalent to equation (3), where the the major difference is that the factor $n(\omega_s)$ in the latter is replaced by αD_m in the former.

We thus selected the spin-up-phase data from table 1, and fitted them with equation (11), over the parameter ranges of $M = 1.0 - 2.4M_{\odot}$ and $R = 8.5 - 15$ km. A result for $D = 6$ kpc and $\alpha D_m = 0.01$ is shown in figure 6, in the same format as figure 4 (but limited to $\dot{P} < 0$). The fit is far from being acceptable, with $\chi_{\nu}^2 = 46$ for 30 DOF. Changing D or αD_m did not solve the problem. This is not surprising, since equation (11) can explain a torque-equilibrium condition ($\dot{P} = 0$) only when the flux tends to zero. This make a contrast to the GL79 model, and disagrees with the measurements. In conclusion, the LRB95 model cannot explain the observed behavior of 4U 1626–67.

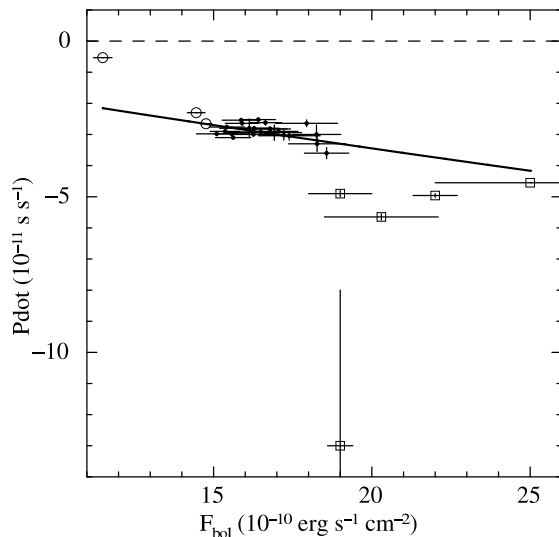


Fig. 6. A scatter plot between \dot{P} and F_{bol} in the spin-up phases, obtained by the MAXI/GSC and other satellites, presented in the same manner as figure 4. The dashed horizontal line indicates $\dot{P} = 0$. The solid line is the best fit model by equation (11), with $M = 1.73M_{\odot}$, $R = 11.1$ km, $D = 6$ kpc, and $\alpha D_m = 0.01$. The fit goodness is $\chi_{\nu}^2 = 46$ (1400/30) for 30 DOF.

5 Discussion

Applying the epoch folding analysis to the MAXI/GSC data, we determined P , \dot{P} , and the X-ray flux of 4U 1626–67 for every 60-d interval from 2009 October to 2013 September. The pulsar has been spinning up throughout this period, and the spin-up rate was positively correlated with the flux.

On the \dot{P} – F_{bol} plane (figure 4), these MAXI/GSC results were confirmed to be fully consistent with those from the past observations (table 1). In fact, the overall data jointly define a well defined \dot{P} vs. F_{bol} correlation, covering rather evenly the spin-up and spin-down phases from $\dot{P} = -6 \times 10^{-11} \text{ s s}^{-1}$ to $+5 \times 10^{-11} \text{ s s}^{-1}$. Utilizing these favorable conditions, we have successfully shown that the accretion-torque theory by GL79 can adequately explain the overall \dot{P} – F_{bol} behavior of 4U 1626–67, while that of LRB95 model cannot explain the data even limiting the comparison to the spin-up phase.

Another favorable condition of this object is the accurate knowledge of its surface magnetic field. As a result, the observed \dot{P} – F_{bol} relation were found to constrain, via the GL79 model, two of the three unknown parameters; the distance D , the mass M of the pulsar, and its radius R . When M and R are allowed to take any value in the nominal mass and radius ranges of neutron stars, namely $M = (1.0 - 2.4) M_{\odot}$ and $R = 8.5 - 15$ km respectively, the distance can be constrained to $D = 5 - 13$ kpc. This is consistent with the limit $D \gtrsim 3$ kpc derived by Chakrabarty et al. (1997); these authors analyzed the \dot{P} behavior of 4U 1626–67 under the assumption of $I = 1 \times 10^{45} \text{ g cm}^2$ and $M = 1.4 M_{\odot}$, then estimated the mass accretion rate to be $\dot{M} \gtrsim 1 \times 10^{16} \text{ g s}^{-1}$ using a similar consideration to the GL79 framework, and compared the expected luminosity to the ob-

served flux. Our distance estimate is also consistent with that of Chakrabarty (1998), 5–13 kpc, which was derived from the optical flux assuming that the effective X-ray albedo of the accretion disk is $\gtrsim 0.9$.

Conversely, if the distance D is assumed, the \dot{P} – F_{bol} relation can fix M and R with relatively small statistical errors. Table 2 lists the allowed M and R ranges for typical source distances assumed. Thus, once D can be determined by some other means, M and R of 4U 1626–67 can be constrained to a rather narrow range, which would be useful to pin-down the nuclear EOS. A point of particular importance is that the present method can provide the information on R , which is more vitally needed than that on M , without not much affected by various systematic errors (figure 5).

In order to further increase the reliability of the GL79 method, it is important to understand the systematic errors (section 3.3). In this respect, an application of the GL79 model to Be X-ray binaries by Klus et al. (2014) is worth noting. They compared the surface magnetic field of these pulsars calculated using the GL79 model ($= B_{\text{GL79}}$), with that measured using cyclotron resonance scattering features ($= B_{\text{C}}$). The ratio was found as $B_{\text{GL79}}/B_{\text{C}} = 3 - 4$ in two examples, GRO J1008–57 and A0535+26. This corresponds to a value of $A \simeq 1.5$, which is consistent with the 50% uncertainty in A assumed in section 3.3. Thus, studying a larger number of sources would be important.

Acknowledgments

The authors are grateful to all members of the MAXI team, BATSE pulsar team and Fermi/GBM pulsar project. This work was supported by RIKEN Junior Research Associate Program, and the Ministry of Education, Culture, Sports, Science and Technology (MEXT), Grant-in-Aid No. 24340041.

Appendix 1 Ghosh & Lamb model

GL79 derived an equation between \dot{P} and L in an X-ray binary pulsar. The accreting matter transfers the angular momentum to the pulsar at the “outer transition zone”, r_0 . Equation (11) in GL79 denotes $r_0 = 0.52 r_{\text{A}}^{(0)}$, where $r_{\text{A}}^{(0)}$ is the characteristic Alfvén radius. Substituting the numbers

$$r_{\text{A}}^{(0)} = 3.2 \times 10^8 \dot{M}_{17}^{-\frac{2}{7}} \mu_{30}^{\frac{4}{7}} \left(\frac{M}{M_{\odot}} \right)^{-\frac{1}{7}} \text{ cm}, \quad (\text{A1})$$

$$r_0 = 1.7 \times 10^8 \dot{M}_{17}^{-\frac{2}{7}} \mu_{30}^{\frac{4}{7}} \left(\frac{M}{M_{\odot}} \right)^{-\frac{1}{7}} \text{ cm}, \quad (\text{A2})$$

where \dot{M}_{17} is the accretion rate \dot{M} in units of 10^{17} g s^{-1} .

GL79 gave their theoretical \dot{P} – L relation [equation (15) in GL79] as

$$\dot{P} = -5.0 \times 10^{-5} \mu_{30}^{\frac{2}{7}} n(\omega_s) S_1(M) P^2 L_{37}^{\frac{6}{7}} \text{ s yr}^{-1}, \quad (\text{A3})$$

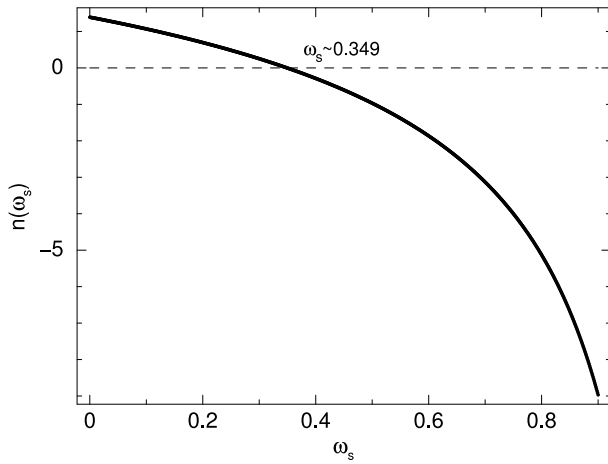


Fig. 7. The function $n(\omega_s)$ with ω_s . The approximation by equation (A4) is effective in $\omega_s = 0 - 0.9$. Thus, $n(\omega_s)$ becomes 0 at $\omega_s \sim 0.349$, is positive in $\omega_s \lesssim 0.349$, and negative in $\omega_s \gtrsim 0.349$.

where L is defined by $L = \dot{M}(GM/R)$. The functions $n(\omega_s)$ and $S_1(M)$ are described respectively by equations (10) and (17) in GL79 as

$$n(\omega_s) \approx 1.39[1 - \omega_s\{4.03(1 - \omega_s)^{0.173} - 0.878\}] \times (1 - \omega_s)^{-1}, \quad (\text{A4})$$

$$S_1(M) = R_6^{\frac{6}{7}} \left(\frac{M}{M_\odot}\right)^{-\frac{3}{7}} I_{45}^{-1}. \quad (\text{A5})$$

Here, ω_s is the so-called fastness parameter, which is a dimensionless parameter, defined as the ratio of the pulsar's angular frequency to the Keplerian angular frequency of the accreting matter. This ω_s is expressed approximately by equation (16) in GL79 as

$$\omega_s \approx 1.35 \mu_{30}^{\frac{6}{7}} S_2(M) P^{-1} L_{37}^{-\frac{3}{7}}. \quad (\text{A6})$$

Here, $S_2(M)$ is given by equation (18) in GL79 as

$$S_2(M) = R_6^{-\frac{3}{7}} \left(\frac{M}{M_\odot}\right)^{-\frac{2}{7}}. \quad (\text{A7})$$

Equation (A4) is accurate to within 5% for $0 \leq \omega_s \leq 0.9$. The behavior of $n(\omega_s)$ is plotted in figure 7, where the zero crossover point is seen to take place at $\omega_s \sim 0.349$.

Appendix 2 Lovelace model

LRB95 introduced magnetic outflows and magnetic braking to explain the relation between \dot{P} and \dot{M} . After many numerical integrations they introduced r_{to} , where the angular velocity ω_a of accreting matter reaches the maximum ($d\omega_a/dr = 0$). The matter transfers the angular momentum to the pulsar at $r = r_{\text{to}}$. r_{to} is given by equation (16) in LRB95 as

$$r_{\text{to}} \approx 0.91 \times 10^8 \left(\frac{\alpha D_m}{0.1}\right)^{0.3} \mu_{30}^{0.57} \dot{M}_{17}^{-0.3} \left(\frac{M}{M_\odot}\right)^{-0.15} \text{cm}. \quad (\text{A8})$$

In LRB95, α is assumed as 0.01 to 0.1 and D_m is order unity. r_{to} has basically the same nature as r_0 in the GL79 model [equation (A2)]. According to r_{to} and r_{cr} , LRB95 demonstrates a magnetic outflow case ($r_{\text{to}} < r_{\text{cr}}$) and magnetic braking of the disk case ($r_{\text{to}} > r_{\text{cr}}$), where r_{cr} is

$$r_{\text{cr}} \equiv \left(\frac{GM}{\omega_*^2}\right)^{\frac{1}{3}} \approx 1.5 \times 10^8 \left(\frac{M}{M_\odot}\right)^{\frac{1}{3}} P^{\frac{2}{3}} \text{cm}, \quad (\text{A9})$$

and $\omega_* = 2\pi/P$.

When r_{to} is smaller than r_{cr} , the pulsar shows spin-up with magnetic outflow. \dot{P} equation [equation (18b) in LRB95] consists \dot{M} and r_{to} . By moving P to the right side,

$$\dot{P} \approx -5.8 \times 10^{-5} P^2 \dot{M}_{17} I_{45}^{-1} \left(\frac{M}{M_\odot}\right)^{\frac{1}{2}} \left(\frac{r_{\text{to}}}{10^8 \text{cm}}\right)^{\frac{1}{2}} \text{s yr}^{-1}. \quad (\text{A10})$$

By deducing $\dot{M} = LR/GM$,

$$\dot{P} \approx -4.3 \times 10^{-5} \mu_{30}^{0.285} \left(\frac{\alpha D_m}{0.1}\right)^{0.15} R_6^{0.85} \times \left(\frac{M}{M_\odot}\right)^{-0.425} I_{45}^{-1} P^2 L_{37}^{0.85} \text{s yr}^{-1}. \quad (\text{A11})$$

It is equivalent to equation (A3). The indices are the same, and the factor is almost the same. The difference is the αD_m term instead of the $n(\omega_s)$ term.

When r_{to} is larger than r_{cr} , magnetic braking takes place. It can work for both spin-up and spin-down, although it mostly works as spin-down.

Appendix 3 Error estimation of period and period derivative

We usually use the folding method to obtain P and \dot{P} of the pulse, orbit etc. First we assume a set of P and \dot{P} , then fold the light curve with them. If there is no periodicity the resultant folded light curve is flat. If there is a pulsation with P and \dot{P} it shows a pulse shape. We calculate χ^2 which is a sum of squared deviation from the mean, to evaluate the existence of a pulse. We change P and \dot{P} to find the most-likely P and \dot{P} which give the maximum χ^2 . We can draw distribution of χ^2 in the P and \dot{P} plane. Figure 3 is an example which we used in this paper to obtain P and \dot{P} of 4U 1626–67. Thus we can derive P and \dot{P} , however, their errors are not obvious.

A.3.1 Method 1 - parameter a and the standard estimate -

The most primitive and straight-forward method for error-estimation is to assume that the errors ΔP , $\Delta \dot{P}$ corresponds to a difference of pulse number a in the whole time span T_s of the observation.

$$\Delta P = \frac{aP^2}{T_s} \quad \Delta \dot{P} = \frac{2aP\dot{P}}{T_s^2} \quad (\text{A12})$$

a is usually less than 1 pulse. Equation (A12) are led by as

follows. The number of pulses $n(t)$ since t_0 is an integral of the pulse frequency $\nu(t)$ from t_0 to t . Let us assume that the frequency ν depends on time with a constant rate $\dot{\nu}$, or we take only the first order of derivatives with time in Taylor expansion series. Using $\nu(t') = \nu_0 + \dot{\nu}_0(t' - t_0)$,

$$n(t) = \int_{t_0}^t \nu(t') dt' = \nu_0(t - t_0) + \frac{\dot{\nu}_0}{2}(t - t_0)^2. \quad (\text{A13})$$

Using the whole time span $T_s = (t - t_0)$,

$$n(t) = \nu_0 T_s + \frac{\dot{\nu}_0}{2} T_s^2. \quad (\text{A14})$$

Equation (A14) is also considered as a function of ν_0 and $\dot{\nu}_0$. We can calculate the ‘‘variation of $n(t)$ ’’, Δn , as a function of variations of $\Delta\nu_0$ and $\Delta\dot{\nu}_0$.

$$\begin{aligned} \Delta n(\Delta\nu_0, \Delta\dot{\nu}_0) &= \frac{\partial n(t)}{\partial \nu_0} \Delta\nu_0 + \frac{\partial n(t)}{\partial \dot{\nu}_0} \Delta\dot{\nu}_0 \\ &= T_s \Delta\nu_0 + \frac{T_s^2}{2} \Delta\dot{\nu}_0 \end{aligned} \quad (\text{A15})$$

In this section we defined $\Delta n = a$, and we obtain $\Delta\nu_0$ and $\Delta\dot{\nu}_0$ from equation (A15).

$$\Delta\nu_0 = \frac{a}{T_s}, \quad \Delta\dot{\nu}_0 = \frac{2a}{T_s^2} \quad (\text{A16})$$

Converting $\Delta\nu_0$ and $\Delta\dot{\nu}_0$ to ΔP_0 and $\Delta\dot{P}_0$ in equation (A16),

$$\Delta P_0 = \frac{a P_0^2}{T_s}, \quad \Delta\dot{P}_0 = \frac{2a P_0^2}{T_s^2} + \frac{2a P_0 \dot{P}_0}{T_s}. \quad (\text{A17})$$

The second term of $\Delta\dot{P}_0$ can be ignored for $P_0/T_s \gg \dot{P}_0$. In our case, we can ignore the term.

In this appendix, we describe various methods with the a value. Leahy (1987) called $a = 1/2$ as the ‘‘standard estimate’’ and gave

$$\frac{\Delta P}{P} = \frac{P}{2T_s}. \quad (\text{A18})$$

When we use $a = 1/2$ in our case ($T_s = 60 \text{ days} = 5184000 \text{ s}$, and $P = 7.67 \text{ s}$), the errors of P and \dot{P} are

$$\Delta P = 5.7 \times 10^{-6} \text{ s}, \quad \Delta\dot{P} = 2.2 \times 10^{-12} \text{ s s}^{-1}. \quad (\text{A19})$$

However, there is no reason to choose $a = 1/2$.

A.3.2 Method 2 - sinusoidal pulse -

It seems natural to consider that a should be related to the reduced chi-square (χ_ν^2) value of the folded light curve. Through the Monte-Carlo simulation, Leahy (1987) obtained an empirical relation between a and χ_ν^2 for a sinusoidal pulse shape as

$$\frac{\Delta P}{\Delta P_L} = 0.71 (\chi_\nu^2 - 1)^{-0.63}, \quad (\text{A20})$$

where $\Delta P_L = P^2/2T_s$. Or, in our notation,

$$a = \frac{1}{2} \times 0.71 (\chi_\nu^2 - 1)^{-0.63}. \quad (\text{A21})$$

The equation is valid within $\chi_\nu^2 = 3 - 110$ which they investigated. In 4U 1626–67, $\chi_\nu^2 = 3.48$ and we can use equation

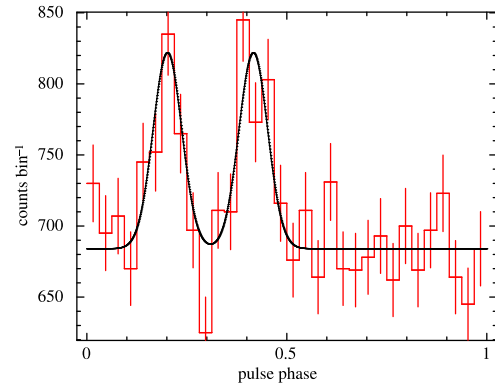


Fig. 8. Observed pulse shape in MJD 55290–55350 and a pulse model in 2–10 keV band. The model consists two gaussian peaks and a constant. Two gaussians have an equal height and an equal width ($\sigma = 0.036$, or FWHM = 0.085). $\chi_\nu^2 = 1.30$. The background rate is 440 counts/bin.

(A21). Then equation (A21) gives $a = 0.20$. By using equation (A17), the error of P is

$$\Delta P = 2.3 \times 10^{-6} \text{ s}. \quad (\text{A22})$$

The error of \dot{P} was not given in Leahy (1987). However, if we assume that a value by equation (A21) might also be effective to calculate the error of \dot{P} ,

$$\Delta\dot{P} = 0.88 \times 10^{-12} \text{ s s}^{-1}. \quad (\text{A23})$$

A.3.3 Method 2 modified - considering the pulse shape -

In method 2, the pulse shape is expressed by a sine function. This can be considered as the worst case among various pulse shapes, since it has the broadest pulse width as wide as 0.5 (FWHM) in phase. In 4U 1626–67, however, the pulse width is as sharp as 0.085 in phase (figure 8). Sharper the pulse shape is, better the period would be determined. Therefore, the error of 4U 1626–67 would also become 0.085/0.5 of that in method 2 ($a = 0.20 \times 0.085/0.5 = 0.034$). Thus

$$\Delta P = 0.39 \times 10^{-6} \text{ s}, \quad \Delta\dot{P} = 0.15 \times 10^{-12} \text{ s s}^{-1}. \quad (\text{A24})$$

Here we ignore the effect that the pulse shape has two peaks.

A.3.4 Method 3 - deviation from the best pulse profile -

If we establish a good fit-model to the pulse profile and χ_ν^2 is about 1.0, we could apply chi-square method to obtain errors of P and \dot{P} . We should note that χ^2 of the fitting to the folded light curve is different from χ^2 of the fitting of the observed light curve by repeating pulse shape model. First, we determine the best-fit model for the folded pulse shape as figure 8. Let us make the model to fit the data acceptably well, and fix it. Then, we vary P to the point where the fit of the model to the data is

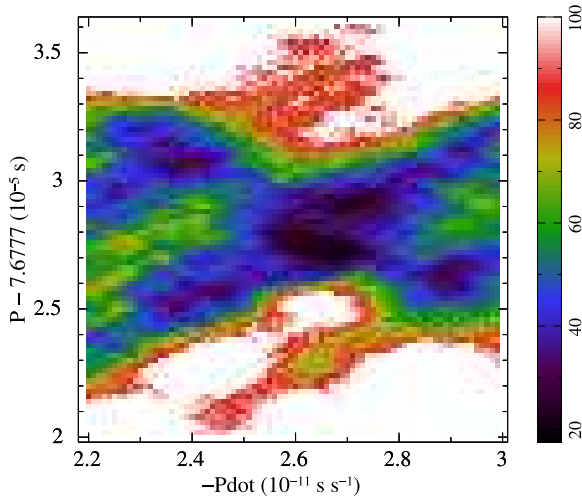


Fig. 9. Distribution of χ^2 which represents deviation for the best pulse model (Method 3). The right bar indicates the χ^2 values. The minimum of χ^2 is 17.48.

no longer acceptable. We take the difference from the best-fit as an error, ΔP . Likewise for \dot{P} . Figure 9 shows a distribution of χ^2 . Here χ^2 has the minimum around the center and it becomes larger as it goes apart. By using the area where χ^2 is the minimum plus 1.0, we obtained the one-parameter error of each P and \dot{P} .

$$\Delta P = 0.2 \times 10^{-6} \text{ s} \quad \Delta \dot{P} = 0.4 \times 10^{-12} \text{ s s}^{-1} \quad (\text{A25})$$

We calculate back that a is 0.02 and 0.09 for P and \dot{P} , respectively.

A.3.5 Method 4 - Monte-Carlo simulation -

We carry out a Monte-Carlo simulation for the X-ray photons and the background taking into account all the observational conditions, such as source intensity, background intensity, accumulated area, exposure, and times of the scans. Using simulated events, we obtain the most-likely P and \dot{P} by the folding method just as we did for the real observation. Figure 10 shows an example of distribution of χ^2 obtained by simulated data. The χ^2 values and the extension are similar to the real case (figure 3). Then we repeat it many (~ 100) times and make a histogram of each resultant P and \dot{P} in figure 11. The errors of P and \dot{P} are given by the gaussian widths (1σ) of the histograms.

$$\Delta P = 0.48 \times 10^{-6} \text{ s} \quad \Delta \dot{P} = 0.63 \times 10^{-12} \text{ s s}^{-1} \quad (\text{A26})$$

We calculate back that a is 0.042 and 0.14 for P and \dot{P} , respectively.

A.3.6 Discussion

We estimated the errors (ΔP , $\Delta \dot{P}$) of P and \dot{P} in the folding by several trial methods. The test case was the MAXI observation

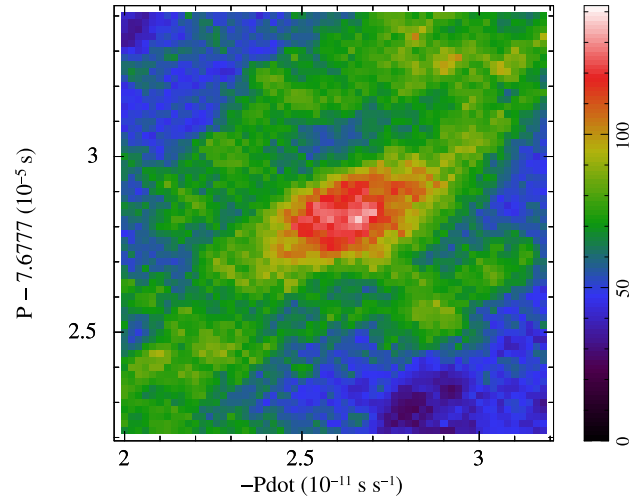


Fig. 10. Distribution of χ^2 of folded pulse profiles on trial P and \dot{P} , calculated for simulated event data in the same observation condition as that in MJD 55290–55350. The right bar indicates the χ^2 values. The maximum χ^2 is 137 for 31 degrees of freedom at $P = 7.6777282 \text{ s}$ and $\dot{P} = -2.66 \times 10^{-11} \text{ s s}^{-1}$.

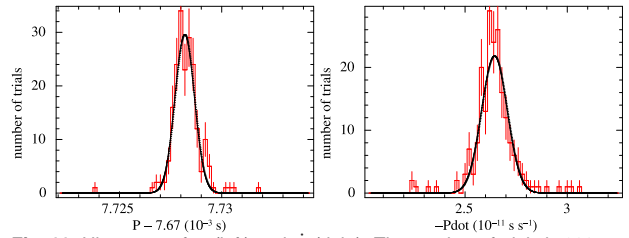


Fig. 11. Histogram of P (left) and \dot{P} (right). The number of trials is 200.

of 4U 1626–67 from MJD 55290 to MJD 55350. The results are tabulated in table 3 and plotted in figure 12. We finally trust the values by the Monte-Carlo simulation (Method 4). Comparing to that, the ΔP value of Method 2 would be only appropriate if the pulse shape is sinusoidal. Since the real pulse shapes are sharper than it, it can be a “loose error” or a conservative error. When we consider sharpness of the pulse shape (Method 2 modified), we get closer value, although it is not exactly the same as the true value. However, on $\Delta \dot{P}$, Method 2 gives the closest value. Since the validity to use the same a as ΔP to estimate $\Delta \dot{P}$ is not clear, the reason why the sinusoidal case (Method 2) gives good value is not known. The Monte-Carlo simulation (Method 4) gives 3 times larger a for $\Delta \dot{P}$ than for ΔP , the reason of which is also unclear. We compare those methods in other span (MJD 56250–56310) as listed in table 4. The relation of a for ΔP in Method 4 and for $\Delta \dot{P}$ is almost the same.

References

- Akmal, A., Pandharipande, V. R., & Ravenhall, D. G. 1998, Phys. Rev. C, 58, 1804
 Angelini, L., White, N. E., Nagase, F., et al. 1995, ApJL, 449, L41

Table 3. Errors of P and \dot{P} in MJD 55290–55350.

Method	ΔP (10^{-6} s)	$\Delta \dot{P}$ (10^{-12} s s $^{-1}$)	a
1 “standard”	5.7	2.2	0.5
2 Leahy	2.3	(0.88)*	0.20
2 modified	0.39	(0.15)*	0.034
3 pulse fit	0.2	0.4	0.02 [†] , 0.09 [‡]
4 MC	0.48	0.63	0.042 [†] , 0.14 [‡]

* $\Delta \dot{P}$ is not given in Leahy (1987).

[†] Calculated from P .

[‡] Calculated from \dot{P} .

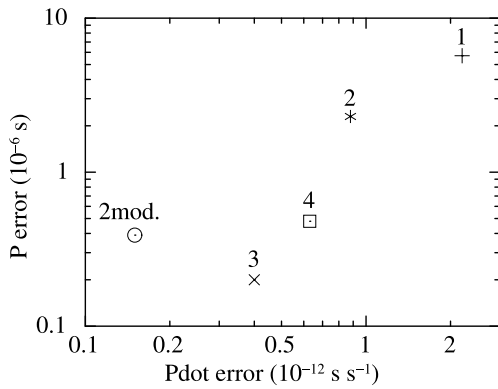


Fig. 12. Errors of P and \dot{P} obtained by various methods. The methods are indicated by the numbers in the figure.

Table 4. Errors of P and \dot{P} in MJD 56250–56310.

Method	ΔP (10^{-6} s)	$\Delta \dot{P}$ (10^{-12} s s $^{-1}$)	a
1 “standard”	5.7	2.2	0.5
2 Leahy	3.3	(1.3)*	0.29
2 modified	0.56	(0.21)*	0.049
3 pulse fit [†]	–	–	–, –
4 MC	0.90	1.07	0.079 [‡] , 0.24 [§]

* $\Delta \dot{P}$ is not given in Leahy (1987).

[†] χ^2 minimum region could not be determined.

[‡] Calculated from P .

[§] Calculated from \dot{P} .

Basko, M. M., & Sunyaev, R. A. 1975, *A&A*, 42, 311
 Bhattacharyya, S. 2010, *Advances in Space Research*, 45, 949
 Bildsten, L., Chakrabarty, D., Chiu, J., et al. 1997, *ApJS*, 113, 367
 Camero-Arranz, A., Finger, M. H., Ikhsanov, N. R., Wilson-Hodge, C. A., & Beklen, E. 2010, *ApJ*, 708, 1500
 Camero-Arranz, A., Pottschmidt, K., Finger, M. H., et al. 2012, *A&A*, 546, AA40
 Chakrabarty, D. 1998, *ApJ*, 492, 342
 Chakrabarty, D., Bildsten, L., Grunsfeld, J. M., et al. 1997, *ApJ*, 474, 414
 Douchin, F., & Haensel, P. 2001, *A&A*, 380, 151
 Elsner, R. F., Darbro, W., Leahy, D., et al. 1983, *ApJ*, 266, 769
 Finger, M. H., Wilson, R. B., & Chakrabarty, D. 1996, *A&AS*, 120, 209
 Ghosh, P., & Lamb, F. K. 1979, *ApJ*, 234, 296
 Giacconi, R., Murray, S., Gursky, H., et al. 1972, *ApJ*, 178, 281
 Iwakiri, W. B., Terada, Y., Mihara, T., et al. 2012, *ApJ*, 751, 35
 Jain, C., Paul, B., & Dutta, A. 2010, *MNRAS*, 403, 920
 Joss, P. C., & Rappaport, S. A. 1984, *ARA&A*, 22, 537
 Kii, T., Hayakawa, S., Nagase, F., Ikegami, T., & Kawai, N. 1986, *PASJ*, 38, 751
 Kirsch, M. G., Briel, U. G., Burrows, D., et al. 2005, *Proc. SPIE*, 5898, 22
 Klochkov, D., Staubert, R., Postnov, K., Shakura, N., & Santangelo, A. 2009, *A&A*, 506, 1261
 Klus, H., Ho, W. C. G., Coe, M. J., Corbet, R. H. D., & Townsend, L. J. 2014, *MNRAS*, 437, 3863
 Krauss, M. I., Schulz, N. S., Chakrabarty, D., Juett, A. M., & Cottam, J. 2007, *ApJ*, 660, 605
 Lattimer, J. M., & Schutz, B. F. 2005, *ApJ*, 629, 979
 Leahy, D. A. 1987, *A&A*, 180, 275
 Levine, A., Ma, C. P., McClintock, J., et al. 1988, *ApJ*, 327, 732
 Lovelace, R. V. E., Romanova, M. M., & Bisnovatyi-Kogan, G. S. 1995, *MNRAS*, 275, 244
 Matsuoka, M., Kawasaki, K., Ueno, S., et al. 2009, *PASJ*, 61, 999
 Mavromatakis, F. 1994, *A&A*, 285, 503
 Mihara, T. 1995, Ph.D. Thesis, Dept. of Physics, Univ. of Tokyo
 Mihara, T., Nakajima, M., Sugizaki, M., et al. 2011, *PASJ*, 63, 623
 Orlandini, M., Dal Fiume, D., Frontera, F., et al. 1998, *ApJL*, 500, L163
 Özel, F. 2013, *Reports on Progress in Physics*, 76, 016901
 Pravdo, S. H., White, N. E., Boldt, E. A., et al. 1979, *ApJ*, 231, 912
 Rappaport, S., & Joss, P. C. 1977, *Nature*, 266, 683
 Rappaport, S., Markert, T., Li, F. K., et al. 1977, *ApJL*, 217, L29
 Reynolds, A. P., Parmar, A. N., Stollberg, M. T., et al. 1996, *A&A*, 312, 872
 Shakura, N. I., & Sunyaev, R. A. 1973, *A&A*, 24, 337
 Shen, H., Toki, H., Oyamatsu, K., & Sumiyoshi, K. 1998a, *Nuclear Physics A*, 637, 435
 Shen, H., Toki, H., Oyamatsu, K., & Sumiyoshi, K. 1998b, *Progress of Theoretical Physics*, 100, 1013
 Shinoda, K., Kii, T., Mitsuda, K., et al. 1990, *PASJ*, 42, L27
 Sugizaki, M., Mihara, T., Serino, M., et al. 2011, *PASJ*, 63, 635
 Sugizaki, M., Yamamoto, T., Mihara, T., Nakajima, M., & Makishima, K. 2015, *PASJ*, 210
 van Haften, L. M., Voss, R., & Nelemans, G. 2012, *A&A*, 543, A121
 Vaughan, B. A., & Kitamoto, S. 1997, *arXiv:astro-ph/9707105*
 Yagi, K., & Yunes, N. 2013, *Phys. Rev. D*, 88, 023009